agronomy

MDPI

Article

Research on Ground-Based Remote-Sensing Inversion Method for Soil Salinity Information Based on Crack Characteristics and Spectral Response

Xiaozhen Liu, Zhuopeng Zhang, Mingxuan Lu, Yifan Wang and Jianhua Ren *

College of Geographical Science, Harbin Normal University, Harbin 150025, China; liuxiaozhen@stu.hrbnu.edu.cn (X.L.); zhuopeng06@stu.hrbnu.edu.cn (Z.Z.); lumingxuan@stu.hrbnu.edu.cn (M.L.); wangyifan225@stu.hrbnu.edu.cn (Y.W.)
* Correspondence: renjianhua@hrbnu.edu.cn; Tel.: +86-431-85542227

Abstract: The precise quantification of soil salinity and the spatial distribution are paramount for proficiently managing and remediating salinized soils. This study aims to explore a pioneering methodology for forecasting soil salinity by combining the spectroscopy of soda saline–alkali soil with crack characteristics, thereby facilitating the ground-based remote-sensing inversion of soil salinity. To attain this objective, a surface cracking experiment was meticulously conducted under controlled indoor conditions for 57 soda saline–alkali soil samples from the Songnen Plain of China. The quantitative parameters for crack characterization, encompassing the length and area of desiccation cracks, together with the contrast texture feature were methodically derived. Furthermore, spectral reflectance of the cracked soil surface was measured. A structural equation model (SEM) was then employed for the estimation of soil salt parameters, including electrical conductivity ($EC_{1:5}$), Na^+, pH, HCO_3^-, CO_3^{2-}, and the total salinity. The investigation unveiled notable associations between different salt parameters and crack attributes, alongside spectral reflectance measurements (r = 0.52–0.95), yet both clay content and mineralogy had little effect on the cracking process due to its low activity index. In addition, the presence of desiccation cracks accentuated the overall spectral contrast of salt-affected soil samples. The application of SEMs facilitated the concurrent prediction of multiple soil salt parameters alongside the regression analysis for individual salt parameters. Nonetheless, this study confers the advantage of the swift synchronous observation of multiple salt parameters whilst furnishing lucid interpretation and pragmatic utility. This study helps us to explore the mechanism of soil salinity on the surface cracking of soda saline–alkali soil in the Songnen Plain of China, and it also provides an effective solution for quickly and accurately predicting soil salt content using crack characteristics, which also provides a new perspective for the hyperspectral measurement of saline–alkali soils.

Keywords: soil salinization; spectral response; desiccation crack; texture feature; structural equation modeling

Citation: Liu, X.; Zhang, Z.; Lu, M.; Wang, Y.; Ren, J. Research on Ground-Based Remote-Sensing Inversion Method for Soil Salinity Information Based on Crack Characteristics and Spectral Response. *Agronomy* **2024**, *14*, 1837. https://doi.org/10.3390/agronomy14081837

Academic Editor: Yanbo Huang

Received: 29 June 2024
Revised: 26 July 2024
Accepted: 16 August 2024
Published: 20 August 2024

1. Introduction

Soil salinization represents a widespread global phenomenon associated with soil degradation, posing significant challenges to both agricultural development and ecological stability. China, hosting the world's third-largest area of saline soils spanning 3.69×10^7 hm^2, equivalent to approximately 4.88% of its available land area, is particularly impacted [1]. Among the salt-affected regions in China, the Songnen Plain stands out with a saline–alkali area of 3.73×10^6 hm^2, primarily consisting of sodium bicarbonate and sodium carbonate as the main salt minerals. Due to the relative high clay content and adsorbable cations, the salt-affected soils in the Songnen Plain suffer from a serious desiccation cracking process during water evaporation, suggesting that exploring the relationship between crack extents and salinity levels can therefore help to expeditiously and accurately

obtain soil salinity data, assess the degree of soil salinization, and delineate the extent of salinized soil, which is also pivotal for guiding soil amelioration efforts, optimizing soil land utilization, and safeguarding the local food security.

Field sampling followed by traditional laboratory analysis is considered the most direct method for detecting soil salinity [2,3]. However, these conventional methods are not efficient in providing real-time soil salinity parameters due to their time-consuming testing processes, long measurement periods, and high labor costs. To overcome these limitations, the electromagnetic induction method is commonly employed to determine salt content without physical contact. This method involves measuring the correlation between the primary magnetic field and the induced secondary magnetic field to quickly assess the apparent soil conductivity [4,5]. While electromagnetic induction sensors like the EM-38 are widely used for monitoring soil salinity, soil texture, and other soil properties in the field [6,7], their accuracy is affected by the physical and chemical properties of different soil types, which are also sensitive to environmental influences [8,9]. In contrast, hyperspectral remote-sensing technology offers a powerful and effective approach for monitoring soil salinity. This technique relies on the diagnostic spectroscopy of different salt minerals and utilizes the wide band range and high spectral resolution of hyperspectral sensors [10,11]. Numerous studies have emphasized the significance of hyperspectral remote sensing in extracting and predicting soil salinity levels. These studies have provided valuable insights into the spectral characteristics and sensitive bands associated with different levels of salinity [12–15]. However, it should be noted that previous ground-based spectral measurements have mainly focused on soil samples obtained through sieving (particles with sizes of 2 mm or less), and spectral data derived from large-scale remote-sensing images often encounter mixed pixel issues, limiting their ability to accurately represent the actual surface conditions of salt-affected soils.

Under natural conditions, it is a common occurrence for clayey soil to undergo shrinkage and develop desiccation cracks during the process of water evaporation. This phenomenon is influenced by several soil properties, including soil salinity, clay content, and mineralogy. Specifically, soils with a higher clay content are more susceptible to severe shrinkage deformation, resulting in more prominent desiccation cracks [16–18]. The presence of different clay minerals can also impact swell–shrinkage cracking, as indicated by their respective plasticity indexes. Soils with lower smectite content and higher amounts of kaolinite, illite, and quartz tend to exhibit smaller shrinkage strains [19–21]. Regarding salt-affected soils, soil salinity also has a significant influence on the cracking process of cohesive salt-affected soils. Extensive research has demonstrated that changes in soil physicochemical parameters, specifically the type of salt minerals and the exchangeable sodium percentage, play a crucial role in the cracking process. In a study conducted by Ren et al. [22], the authors utilized a large number of soil samples collected under natural conditions to establish a relationship between the texture features of desiccation cracks and the salinity of soda saline–alkali soils. They employed a four-level orthogonal wavelet decomposition and found that high-frequency texture features, such as energy and the L1 norm, exhibited an exponential correlation with $EC_{1:5}$ values of salt-affected soils. Another study by Zhang et al. [23] focused on predicting the main salt parameters of salt-affected soils in the Songnen Plain of China. They compared three different methods and discovered that total salinity promotes the process of desiccation cracking in soda saline–alkali soils. They also demonstrated that the artificial neural network (ANN) method can accurately predict Na^+ and $EC_{1:5}$ levels. Fujimaki et al. [24] investigated the relationship between the crack characteristics and physicochemical parameters of saline soils. They evaluated $EC_{1:2}$ values in agricultural fields with desiccation cracks in the Nile Delta and found that cracks facilitate the rapid movement of soil salts through water, thereby influencing the distribution of soil salts. Additionally, Zhang et al. [25] conducted a study on pure clay of bentonite and observed that the salt concentration significantly induced and altered the morphology and patterns of desiccation cracks. As the concentration of the sodium chloride (NaCl) solution increased, larger crack lengths and lower crack densities were obtained. In

order to gain a comprehensive understanding of the mechanism underlying desiccation cracking in saline–alkali soil and provide valuable insights for engineering practices, Xing et al. [26] conducted a study wherein they treated soil samples with saturated solutions of NaCl at concentrations of 5 g/L, 50 g/L, and 100 g/L. The results of their experiments demonstrated a gradual decrease in both soil-crack area and crack length with increasing Na^+ concentration. However, an opposite trend was observed for crack number, which increased with increasing Na^+ concentration. Wang et al. [27] suggested different results in their research, wherein NaCl treatments were found to increase both the total area and average width of desiccation cracks in shrink–swell light clays. This discrepancy highlights the complexity of the desiccation cracking process and emphasizes the need for further investigation. Although previous studies have examined the desiccation cracking process under varying salinity conditions, the specific mechanism through which salinity influences the soil-cracking process remains unresolved. This uncertainty may be attributed to the complex interactions between different cations and soil particles, which are influenced by factors such as ion concentration, valence state, topography, climate, and soil type.

Although numerous studies have investigated the effects of soil salinity and salt mineral composition on the cracking process of different salt-affected soils, most of these studies have focused on determining the control of the soil-cracking process and its impact on the extent of soil surface cracking through experimentation with a limited number of sample variations under controlled desiccation cracking conditions. However, there is a lack of research that aims to predict soil salinity in real-world scenarios based on crack characteristics. Furthermore, the hyperspectral characteristics of salt-affected soil, which provide important information about the type and content of soil salt minerals, have not been extensively studied in relation to cracked saline–alkali soil. Additionally, the complexity of cracks can further influence the spectral response of the soil surface, while the crack area can also affect the volume scattering process of electromagnetic radiation. Therefore, integrating crack characteristics and the spectral response through ground-based remote-sensing methods can greatly improve the accuracy of soil salinity content prediction, thereby facilitating soil salinity monitoring. This study attempts to perform desiccation cracking experiments under controlled indoor conditions using soil samples with different salinity levels. Three types of crack parameters, including crack length, crack area, and texture feature, were quantitatively extracted from the crack patterns of soil samples under completely dry conditions. Meanwhile, spectral data of cracked soil samples were also measured in this study. After that, structural equation modeling (SEM) was explored to realize single-parameter and multi-parameter prediction methods for soil salt parameters including $EC_{1:5}$, pH, Na^+, HCO_3^-, CO_3^{2-}, and the total salinity by combing the crack characteristics and spectral responses of cracked saline–alkali soils. This not only enables the effective prediction of salt information in cracked soil from a ground-based remote-sensing perspective but also enhances the experimental process and scheme design for the hyperspectral measurement of saline–alkali soil surfaces. As a result, this study provides valuable data support for local soil remediation efforts and strengthens the remediation of soda saline–alkali soil in the Songnen Plain, China. Furthermore, this approach propels the field of hyperspectral remote sensing for soil salinization monitoring and extends the application of soil hyperspectral remote-sensing technology. Additionally, this research also attempts to improve the experimental process and scheme design for hyperspectral measurement of saline alkali soil surfaces, providing crucial data for local soil remediation efforts and advancing the application of hyperspectral remote sensing for soil salinization monitoring.

2. Materials and Methods

2.1. Study Area

The Songnen Plain is located in the center of Northeast China between the Liao River and the Heilongjiang River, which has a flat topography, low elevation, a high water table and poor drainage. The soils in the western Songnen Plain are highly saline, with $EC_{1:5}$

mainly ranging from 0.04 to 3.99 dS/m [28,29]. Sodium carbonate (Na_2CO_3) and sodium bicarbonate ($NaHCO_3$) are the main salt minerals, and it is commonly known as one of the main areas affected by soil salinization in China and one of the three areas with the highest degree of soda salinization in the world, with a saline soil area of up to 2.55×10^6 hm^2 [30]. A specific city within the Songnen Plain that suffers significantly from salinization is Da'an City located in Jilin Province. This city is situated in the western part of the Songnen Plain and experiences a temperate continental monsoon climate, with an average annual rainfall ranging from 400 to 500 mm, predominantly occurring from July to August. The irregular distribution of this rainfall, coupled with an average annual evaporation rate of 1500–1900 mm, results in a pronounced imbalance between evaporation and precipitation. Consequently, the soil surface exhibits conspicuous shrinkage and cracking due to water evaporation. Furthermore, the poor infiltration capacity of soda–saline soils inhibits the downward movement of salt, thereby rendering the physicochemical properties of the soil surface relatively stable. With consideration given to road accessibility, the heterogeneity of the physicochemical properties of salt-affected soils, and the spatial distribution of soil salinity levels, different regions experiencing desiccation cracking were selected under natural conditions. Each crack region was then set up with several sampling points based on the difference in surface crack states. A total of 57 sampling sites with different salinities were finally selected and recorded using a handheld GPS (Figure 1). After that, all soil samples were collected from 0 to 20 cm, dried, crushed, passed through a 2 mm sieve, and divided into two parts. The first part was used for soil physicochemical property measurements, and the other part was prepared for soil surface cracking experiments and spectroscopy measurements under controlled conditions.

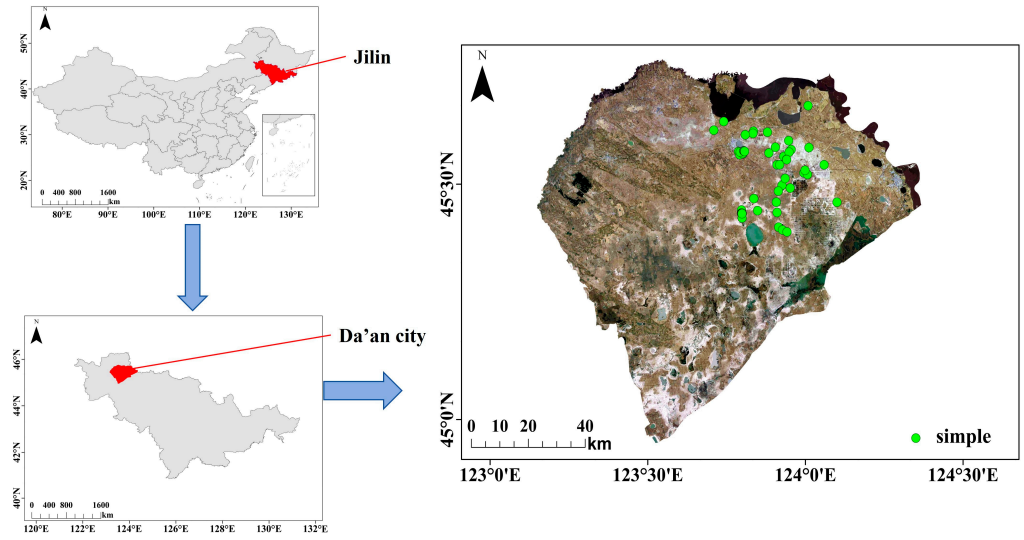

Figure 1. Distribution of research area and sampling points.

2.2. Soil Property Measurements

In this study, all physicochemical parameters of the soil samples, mainly consisting of ion content, pH, soil electrical conductivity (EC), mass soil moisture and soil texture, were analyzed and measured in the laboratory, [31]. The ion contents were all measured using soil extracts with a soil/water mass ratio of 1:5. Specifically, Na^+ and K^+ were measured using the flame photometer method; Ca^{2+} and Mg^{2+} were measured using the EDTA complexation titration method; Cl^- was measured using the silver nitrate ($AgNO_3$) solution titration method; and CO_3^{2-} and HCO_3^- were measured using the double indicator neutralization method. Salinity referred to the sum of all salt ion contents. It should be noted that the SO_4^{2-} content was neglected because the SO_4^{2-} content in the Songnen Plain soils was very limited. The total soil salinity referred to the sum of all ion contents measured above. In this study, both ion contents and the total soil salinity refer

to the proportion of ion contents measured through the soil extraction solution to the dry soil mass of each sample, with the same unit of mg/g. Additionally, $pH_{1:5}$ and $EC_{1:5}$ were determined using a soil suspension with a soil/water mass ratio of 1:5 and was measured based on the potentiometric and conductivity methods, respectively. Moreover, the soil textures of all soil samples were also determined by a Malvern MS-2000 laser particle size analyzer to measure the particle size distributions of clay (0–2 μm), silt (2–50 μm) and sand (50–2000 μm).

2.3. Soil-Cracking Experiment

Before conducting the cracking experiment, the thorough homogenization of the samples was ensured by removing impurities such as grass clippings. To create a well-saturated slurry, water was added to each soil sample, resulting in an initial soil moisture level of 50%. Additionally, the dry weight of each sample was recorded. Taking into account the friction and water permeability of the sample box bottom, square wooden boxes with inner dimensions of 50 cm by 50 cm and a height of 3 cm were prepared. The saturated slurry of each soil sample was then poured into the respective sample box, ensuring a smooth surface. Subsequently, all soil samples were placed in a controlled laboratory environment with a temperature of 25 °C, a humidity of 35%, and a pressure of 101 kPa. These controlled conditions were essential to consistently regulate the water evaporation during the desiccation cracking test. It is noteworthy that the mass soil moisture of each sample was monitored every 12 h during the cracking process by calculating the difference between its dry weight and the measured weight. The experiment was considered complete when the weights of all soil samples no longer decreased [32,33].

2.4. Photography and Spectroscopy of Cracked Soil Samples

Upon the completion of the cracking experiment, standardized measurements were performed on all cracked soil samples (Figure 2). The soil surface with desiccation cracks was photographed and analyzed using spectroscopy (Figure 2a). A high-resolution digital camera was utilized for the photography; it was placed on a height-adjustable platform with the camera lens positioned 1 m vertically above the ground. A fixed square area measuring 50 cm × 50 cm, centered on the projection of the lens, was defined on the ground. The camera was white-balanced and set with a uniform aperture size and exposure time. Afterward, each soil sample was placed within this fixed area and photographed (Figure 2b). To correct for geometric aberration in crack patterns across all soil samples, a checkerboard grid calibration plate was then prepared and photographed under the same conditions (Figure 2c).

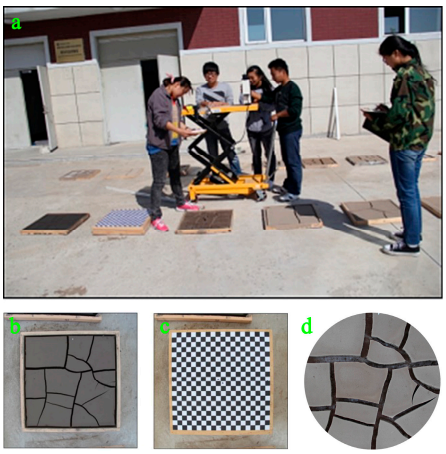

Figure 2. The standardized measurements of photography and spectroscopy of cracked soil samples. (**a**). Measurement process; (**b**). Crack pattern; (**c**). Image of calibration plate; (**d**). Area of spectral irradiation.

The spectral response of cracked saline–alkali soil was acquired using an ASD FieldSpec3 hyperspectral spectrometer with a visible near-infrared detector (VNIR: 350–1000 nm, sampling interval of 1.4 nm, and spectral resolution of 3 nm) and a short-wave infrared detector (SWIR: 1000–2500 nm, sampling interval of 2 nm, and spectral resolution of 10 nm). Spectral measurements were conducted under clear and cloudless weather conditions. Specifically, the spectrometer was fixed on the platform with an optical probe (25° field of view) positioned 1 m above the fixed square area. Each soil sample was then placed within this area, corresponding to a circular region with a diameter of approximately 45 cm (Figure 2d). After that, dark current removal and whiteboard calibration procedures were performed, and 10 spectral reflectance measurements were collected and averaged to account for instrument noise. Finally, the reflectance of each cracked soil sample was resampled at 10 nm intervals to further reduce equipment noise and the dimensionality of the data.

2.5. Extraction of Crack Characteristics

The MATLAB software 2023a was utilized in this study to extract crack parameters from all soil samples that were subjected to cracking. Initially, the calibration plate was geometrically corrected based on the coordinates of the grid intersection positions. A polynomial geometric correction model was then developed [34]. Subsequently, a batch operation of geometric correction was applied to all crack images taken under the same photographic conditions, and the resulting images were cropped accordingly (Figure 3a). Following this, the color images were converted to grayscale by averaging the red, green, and blue components (Figure 3b). It is important to note that, to eliminate the impact of sample frames producing shadows on the image edges, the grayscale images were further cropped to a uniform size of 47.5 cm × 47.5 cm. The crack image was then subjected to binarization and inversion using the threshold determined from the histogram of the grayscale image (Figure 3c). This process indicated that the white areas of the images represented the cracks, while the black areas represented the uncracked soil surface [35]. Finally, skeletonization was performed on each binary image to obtain the crack network with a width of only one pixel [36], and any redundant blurs generated during the skeletonization process were removed (Figure 3d).

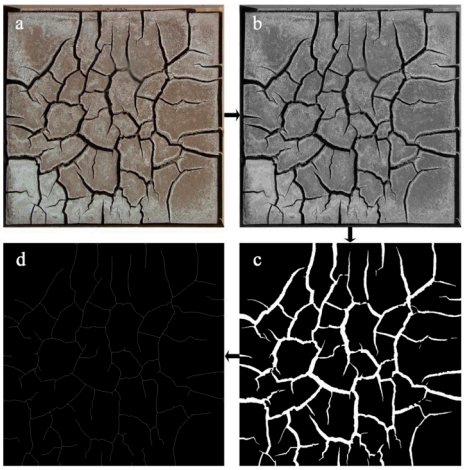

Figure 3. The preprocessing process of crack images. (**a**). Cropped crack image; (**b**). Grayscale crack image; (**c**). Binary crack image; (**d**). Skeletonized crack image.

Crack length (CL) and crack area (CA) are the foundational geometric features characterizing the cracks on the soil surface after pre-processing operations on the crack image. In this study, the actual size of pixel (S) is determined using the length of 47.5 cm and its corresponding pixel number. After that, the CL of each soil samples was calculated by multiplying S and the total number of crack skeletons. After that, the numbers of

both the whole crack image and extracted crack area were used to determine the crack ratio [37,38], which was then used to calculate the CA of each soil sample. In addition, the classical gray level co-occurrence matrix (GLCM) is proposed for the texture features of crack patterns [39,40]. Specifically, the second-order combined conditional probability density of the binary image under different orientations under directions of 0°, 45°, 90° and 135° was calculated for GLCMs, with the formula listed below:

$$p(i,j) = g\{(x_1,y_1),(x_2,y_2) \in m \times n | f(x_1,y_1) = i, f(x_2,y_2) = j\} \quad (1)$$

where i, j denotes the gray values of the gray image $f(x, y)$ at coordinate positions (x_1, y_1) and (x_2, y_2), and $p(i, j)$ refers to the second-order combined conditional probability density. In order to describe the texture state of the image more intuitively, the contrast texture feature (*CON*) of the crack image was calculated to further characterize the clarity of the cracked image [41] and to reflect texture intensity of the neighboring image elements of the cracked image. The *CON* formula is as follows:

$$CON = \sum_{n}^{Ng-1} n^2 \left\{ \sum_{i=1}^{Ng} \sum_{j=1}^{Ng} p(i,j) \right\}, |i-j| = n \quad (2)$$

where Ng represents the number of gray levels in the GLCM. Since the generation and development direction of desiccation cracks are random, the arithmetic means of *CON* calculated from different directions were taken as the final *CON* of the cracked image.

2.6. Structural Equation Model

A structural equation model (SEM) integrates the characteristics of factor analysis and path analysis, which is widely applied in fields such as psychology, education, and finance [42,43]. It provides a powerful tool for identifying, modeling, and explaining relationships among multiple variables, particularly in complex scenarios involving multiple indicators [44]. Due to its unique analytical capability, an SEM is often used for qualitative analysis in the field of geography [45–47], with relatively fewer studies employing quantitative analysis. We note that when it is necessary to describe an abstract concept or phenomenon with multiple indicators using an SEM, these indicators are integrated into latent variables, while the indicators themselves serve as manifest variables. In the framework of an SEM, latent variables can be further classified into both exogenous and endogenous latent variables. Exogenous latent variables can independently influence other variables without being affected by other factors, while endogenous latent variables are influenced by other latent variables or external factors. In this study, crack characteristics and spectral responses are considered as exogenous latent variables, while soil physicochemical properties refer to endogenous latent variables of soil samples. The SEM consists of measurement equations and structural equations, where the measurement model is a prerequisite and foundation of SEM analysis, used to represent the inherent relationships between measurement variables and corresponding endogenous or exogenous latent variables.

The mathematical expression of the exogenous variable equation can be expressed as

$$X = \Lambda_x \xi + \delta \quad (3)$$

where X represents exogenous observed variables. Λ_x is the factor loading matrix between X and ξ. δ is the measurement error term of exogenous variables.

The mathematical expression of the endogenous variable equation can be represented as

$$Y = \Lambda_y \eta + \varepsilon \quad (4)$$

where Y represents exogenous observed variables. Λ_y refers to the factor loading matrix between Y and η. ε is the measurement error term of exogenous variables.

The mathematical expression of the structural model can thus be represented as

$$\eta = B_\eta + \Gamma\xi + \zeta \quad (5)$$

where ξ and η refer to exogenous and endogenous latent variables, respectively. B_η is the factor loading between endogenous latent variables. Γ represents the relationship matrix between ξ and η. ζ refers to the residual error term of the structural equation [48]. The schematic diagram of the structural equation model is shown in Figure 4.

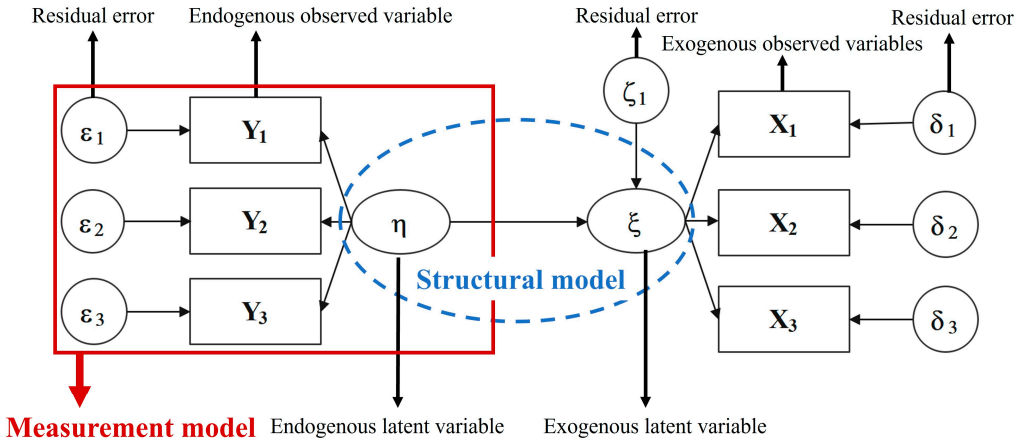

Figure 4. SEM schematic diagram.

2.7. Correlation Analysis

In order to quantitatively analyze the relationships between the different crack characteristics, spectral responses and physicochemical parameters of soda saline–alkali soils, the following formulas were utilized in this study to calculate the Pearson correlation coefficients between the main physicochemical parameters (pH, $EC_{1:5}$, Na^+, HCO_3^-, CO_3^{2-}, salinity) and crack feature parameters of the saline soils in the Songnen Plain. This was in addition to the correlation coefficients between the main physicochemical parameters of the soil and spectral reflectance [49].

$$R = \frac{\sum_{i=1}^{n}(x_i - \overline{x}) \times (y_i - \overline{y})}{\sqrt{\sum_{i=1}^{n}(x_i - \overline{x}) \times \sum_{i=1}^{n}(y_i - \overline{y})}} \quad (6)$$

where R is the Pearson correlation coefficient calculation result, x_i refers to the measured soil salt parameters, y_i describes the crack feature parameters or spectral reflectance, and n represents the number of soil samples.

3. Results

3.1. Physicochemical Parameters

The statistical results of the main salt parameters are shown in Table 1. The table indicates that the pH of the soil samples ranged from 8.01 to 10.77, while $EC_{1:5}$ ranged from 0.06 dS/m to 3.39 dS/m, suggesting that all soil samples exhibited obvious alkaline characteristics. Additionally, Table 1 also shows that contents of Na^+, HCO_3^-, CO_3^{2-}, and soil salinity covered from 0.12 to 14.12 mg/g, 0.15 to 4.99 mg/g, 0 to 5.51 mg/g, and 11.06 to 29.73 mg/g, respectively, indicating quite a large distribution. The coefficient of variation exceeding 63.40% indicated a considerable degree of dispersion among the salt parameters of the samples, which also suggested the wide coverage of the samples and significant differences in salt parameters. The soil moisture of all soil samples after the drying process covered a range from only 2.04% to 4.31% with an average value of 2.97%,

suggesting that the desiccation cracking is well completed. Table 1 also indicates that the soil samples belong to a typical soil texture of clay loam, according to the soil taxonomy proposed by the United States Department of Agriculture (USDA).

Table 1. Statistical description of soil properties.

Soil Parameters	Min	Max	Mean	SD	CV (%)	Skewness	Kurtosis
pH	8.01	10.77	9.83	0.73	7.41	−1.14	0.18
$EC_{1:5}$ (dS/m)	0.06	3.39	0.97	0.84	86.64	1.02	0.56
Na^+ (mg/g)	0.12	14.12	3.32	3.28	98.95	1.51	2.13
K^+ (mg/g)	0.01	0.06	0.02	0.01	67.41	2.14	5.49
Ca^{2+} and Mg^{2+} (mg/g)	0.10	1.60	0.53	0.32	59.75	1.19	1.67
HCO_3^- (mg/g)	0.12	5.00	1.57	0.99	63.4	1.11	1.38
CO_3^{2-} (mg/g)	0	5.50	1.75	1.56	89.33	1.02	0.14
Cl^- (mg/g)	0.08	5.25	1.32	1.46	110.44	1.34	0.86
Salinity (mg/g)	1.06	29.73	8.50	6.46	75.98	1.22	1.43
Soil moisture (%)	2.04	4.31	2.97	0.58	19.65	0.15	−1.12
Clay (%)	25.39	32.04	27.98	1.54	5.49	0.43	−0.27
Silt (%)	28.72	40.4	35.19	3.18	9.03	−0.12	−0.82
Sand (%)	28.26	43.94	36.85	3.64	9.87	−0.21	−0.85

N = 57, SD: standard deviation, CV: coefficient of variation.

3.2. Crack Characteristics

Table 2 shows the crack characteristics obtained from the soil samples following the drying process. The results revealed a wide range of crack parameters for CL, ranging from 200.00 cm to 797.18 cm, and for CA, ranging from 36.78 cm^2 to 547.54 cm^2. These findings indicated significant differences in the geometric crack characteristics among various soil samples. In addition, CON covered a range from 1.14 to 1.64, fully suggesting the contrast of the adjacent images and the strength of the texture feature.

Table 2. Statistical results of three crack characteristic parameters of all cracked soil samples.

Soil Parameters	Min	Max	Mean	SD	CV (%)	Skewness	Kurtosis
CL (cm)	200.00	797.18	444.26	120.65	27.16	0.54	0.58
CA (cm^2)	36.78	547.54	311.80	130.80	41.95	−0.08	−0.78
CON	1.14	1.6	1.44	0.12	8.6	−0.8	−0.24

N = 57, SD: standard deviation, CV: coefficient of variation.

3.3. Spectral Responses

Figure 5 depicts the spectral characteristics of soil samples with different salinity levels; it was drawn based on 11 samples evenly selected by salinity intervals. It is observed from the figure that the spectral reflectance curves of the different soda salinized soil samples were essentially the same in shape. Specifically, the reflectance showed a clear increasing trend from 350 to 1400 nm. Subsequently, the growth rate of the reflectance curves in the 1400–1800 nm band range slowed down, and the curves were close to parallel. Between 1800 and 1850 nm, the spectral features changed sharply due to the influence of atmospheric water content. In addition, the reflectance curves in the range of 1850–2350 nm showed a trend of first increasing and then decreasing, with a peak appearing at approximately 2100 nm.

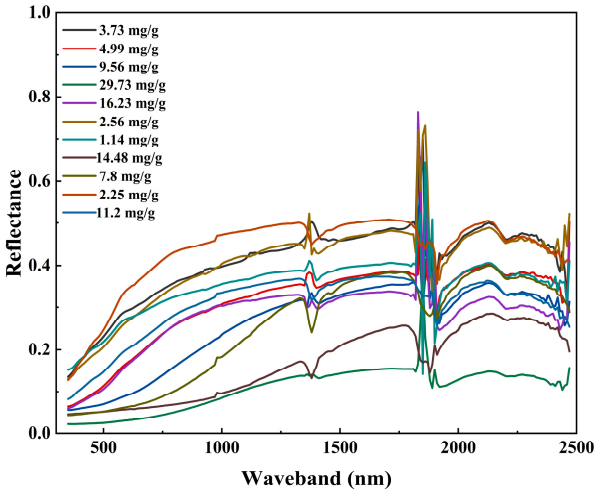

Figure 5. Spectral characteristics of 11 soil samples with different soil salinity.

Figure 6 shows the absolute values of the correlation coefficients between spectral reflectance and six main salt parameters, indicating that the curves of $EC_{1:5}$, Na^+, HCO_3^-, and salinity were similar in shape. Specifically, there was an increasing trend below 1400 nm, with a smaller peak near 500 nm. In the range of 1400–1900 nm, the correlation of the values of soil physicochemical parameters showed a decreasing and then increasing trend, but the magnitude of the change was not significant. In addition, the correlation coefficient curves showed a weak peak near 1900 nm followed by a slow decrease. The correlation coefficient curves of reflectance of CO_3^{2-} and pH showed a clear decreasing trend between 500 and 1400 nm and a small absorption valley near 1000 nm. In the range of 1400–2500 nm, the correlation curves of HCO_3^- versus pH showed a slow decrease followed by an increase and then another decrease. It can also be found from the figure that the correlation curve of pH was much lower than that with HCO_3^-. Therefore, the maximum values of the correlation coefficients between different salt parameters and reflectance can be seen in the vicinity of the 1990 nm band.

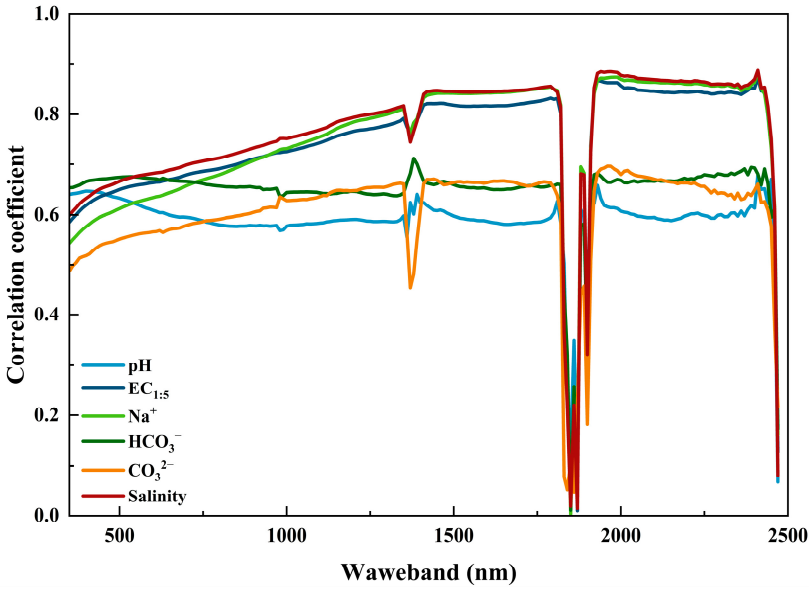

Figure 6. Correlograms between reflectance and main soil properties of soil samples.

The reflectance at 1990 nm of 57 soil samples was extracted as the spectral parameter in the prediction model. Table 3 shows the statistical characteristics of reflectance at 1990 nm for all samples. It can be seen that the reflectance of different samples covered a large range

of variation, and the CV of 21.17% indicates that the reflectance of different samples at 1990 nm had a large degree of dispersion, suggesting that there was a large variation in the reflectance of different samples in this band.

Table 3. Statistical results of spectral characteristics of all cracked soil samples.

	Min	Max	Mean	SD	CV (%)	Skewness	Kurtosis
1990 nm	0.11	0.47	0.36	0.08	21.17	−0.9	0.85

N = 57.

3.4. Correlation Coefficients

Table 4 displays the cross-correlations among different soil parameters and crack characteristics and the spectral reflectance of all 57 soil samples. It can be seen that the main soil salt parameters were positively correlated with all crack parameters but negatively correlated with spectral reflectance. Table 4 also shows that soil physicochemical parameters had the strongest overall correlation with CON, with correlation coefficients ranging from 0.65 to 0.95. However, the overall correlation between salt parameters and CA was the lowest, with correlation coefficients ranging only from 0.31 to 0.55. In addition, Na^+ had the strongest correlation with spectral reflectance with a correlation coefficient of −0.89, but pH had the poorest response to spectral reflectance with a correlation coefficient of −0.56. At the same time, the correlation of different cleavage features and spectral reflectance with soil salinity basically satisfied the relationship of pH < HCO_3^- < CO_3^{2-} < Na^+ < $EC_{1:5}$ < salinity. Moreover, the poor correlation coefficients from only 0.13 to 0.25 in Table 4 also shows that the clay content had very little effect on desiccation cracks.

Table 4. Correlation coefficient matrix of salt parameters with crack characteristics and spectral reflectance.

	CL (cm)	CA (cm^2)	CON	Reflectance
pH	0.66 **	0.45 **	0.65 **	−0.56 **
$EC_{1:5}$ (dS/m)	0.92 **	0.55 **	0.94 **	−0.88 **
Na^+ (mg/g)	0.91 **	0.50 **	0.93 **	−0.89 **
HCO_3^- (mg/g)	0.62 **	0.47 **	0.61 **	−0.66 **
CO_3^{2-} (mg/g)	0.76 **	0.31 **	0.74 **	−0.73 **
Salinity (mg/g)	0.94 **	0.52 **	0.95 **	−0.92 **
Clay (%)	0.14	0.26 *	0.13	−0.05

N = 57, CL: Crack length, CA: Crack area; **: the significant level of correlation at $p \leq 0.01$; *: the significant level of correlation at $p \leq 0.05$.

3.5. Prediction Models of Salt Parameters

In this study, a modeling set of 40 samples and a validation set of 17 samples were randomly generated in a 2:1 ratio, gradient by gradient, according to the arranged numerical order of soil salinity. The CL, CA, CON, and reflectance in the 1990 nm range were selected as independent variables. An SEM was then developed and validated. Among them, the SEM of salt parameters was divided into simultaneous models for many-to-many and individual models for many-to-one.

3.5.1. Multi-Parameter Prediction of SEMs

Table 5 shows the simultaneous modeling of different salt parameters using an SEM. From the table, it can be seen that the modeling accuracy of $EC_{1:5}$ and Na^+ was the highest, with an R^2 of 0.92 and an RPD above 2. The modeling accuracy of salinity was also good, with an R^2 of 0.9 and an RPD above 2. Thereafter, the model was able to capture the intrinsic relationship of the data to a large extent and can be used to predict the salinity, $EC_{1:5}$ and Na^+. Additionally, the prediction R^2 of CO_3^{2-} is 0.53, indicating that the model is able to explain more than half of the observed variance. However, the modeling accuracy of

the SEM for HCO_3^- and pH was very low, with an R^2 of only 0.46 and 0.41, respectively. Furthermore, the relative RPDs for the final three parameters are all less than 2, which provides additional evidence that the model has limited predictive power with regard to these parameters.

Table 5. Structural equation models for predicting different salt parameters simultaneously.

Soil Salt Parameters	Formulas	R^2	RPD	RMSE	MAE
pH	$Y = 10.266 + 0.265\ X_1 + 0.300\ X_2 + 0.271\ X_3 - 0.254\ X_4$	0.41	1.08	0.95	0.56
$EC_{1:5}$ (dS/m)	$Y = 3.061 + 0.461\ X_1 + 0.303\ X_2 + 0.471\ X_3 - 0.451\ X_4$	0.92	2.15	0.28	0.73
Na^+ (mg/g)	$Y = 3.676 + 1.782\ X_1 + 0.925\ X_2 + 1.820\ X_3 - 1.709\ X_4$	0.92	2.11	0.36	2.65
HCO_3^- (mg/g)	$Y = 2.123 + 0.386\ X_1 + 0.253\ X_2 + 0.395\ X_3 - 0.377\ X_4$	0.46	1.08	0.66	1.16
CO_3^{2-} (mg/g)	$Y = 3.823 + 0.713\ X_1 + 0.468\ X_2 + 0.729\ X_3 - 0.697\ X_4$	0.53	1.05	0.99	1.50
Salinity (mg/g)	$Y = 10.823 + 16.797\ X_1 + 11.030\ X_2 + 17.124\ X_3 - 16.084\ X_4$	0.90	2.14	1.98	2.67

N = 40, X_1: Crack length (CL), X_2: Crack area (CA), X_3: CON, X_4: Reflectance at 1990 nm.

3.5.2. Single-Parameter Prediction of SEMs

Table 6 presents the prediction results of an SEM for different salt parameters modeled separately by single parameters. From the table, it can be seen that the prediction accuracy of $EC_{1:5}$, Na^+, and salinity was high with an R^2 of 0.91, 0.91, and 0.94, and the RPD of these three parameters was above 2. Subsequently, the R^2 of predicted CO_3^{2-} was 0.62, suggesting that the single-parameter prediction of structural equation modeling also had a certain prediction ability. However, the SEM did not predict pH and HCO_3^- well, with R^2 scores of only 0.41 and 0.48, respectively. Moreover, the relative RPD for the final three parameters was less than 2, suggesting that these salt parameters were predicted with limited stability.

Table 6. Structural equation models for predicting different salt parameters separately.

Soil Salt Parameters	Formulas	R^2	RPD	RMSE	MAE
pH	$Y = 10.274 + 0.261\ X_1 + 0.177\ X_2 + 0.269\ X_3 - 0.247\ X_4$	0.41	1.10	1.12	0.80
$EC_{1:5}$ (dS/m)	$Y = 3.037 + 0.457\ X_1 + 0.309\ X_2 + 0.471\ X_3 - 0.438\ X_4$	0.91	2.18	0.30	0.83
Na^+ (mg/g)	$Y = 8.676 + 1.751\ X_1 + 1.167\ X_2 + 1.816\ X_3 - 1.677\ X_4$	0.91	2.15	0.39	2.54
HCO_3^- (mg/g)	$Y = 1.566 + 0.367\ X_1 + 0.249\ X_2 + 0.379\ X_3 - 0.379\ X_4$	0.48	1.14	0.60	1.02
CO_3^{2-} (mg/g)	$Y = 3.406 + 0.671\ X_1 + 0.459\ X_2 + 0.699\ X_3 - 0.643\ X_4$	0.62	1.08	0.97	1.47
Salinity (mg/g)	$Y = 13.889 + 3.6463\ X_1 + 2.390\ X_2 + 3.720\ X_3 - 3.559\ X_4$	0.94	2.66	2.11	2.47

N = 40, X_1: Crack length (CL), X_2: Crack area (CA), X_3: CON, X_4: Reflectance at 1990 nm.

3.5.3. Verification of Prediction Models

In order to validate the accuracy of salt parameters, scatter plots were drawn versus predicted and measured salt parameters for soil samples in the validation set. Figures 7 and 8 display the results of the SEM for single-parameter and multi-parameter prediction, respectively. The red areas in the figures showed the confidence intervals of the fitted data. It was evident that the single-parameter structural equation modeling exhibited superior fitting outcomes regardless of the salt parameters compared with the prediction results of multiple parameters. For different salt parameters, the confidence intervals of total salinity and Na^+ can basically cover y = x. In addition, the confidence intervals of $EC_{1:5}$ also overlapped with y = x to a certain extent. In addition, it can be seen from both figures that although the CO_3^{2-} validation performance is poor, it was still better than HCO_3^- and pH.

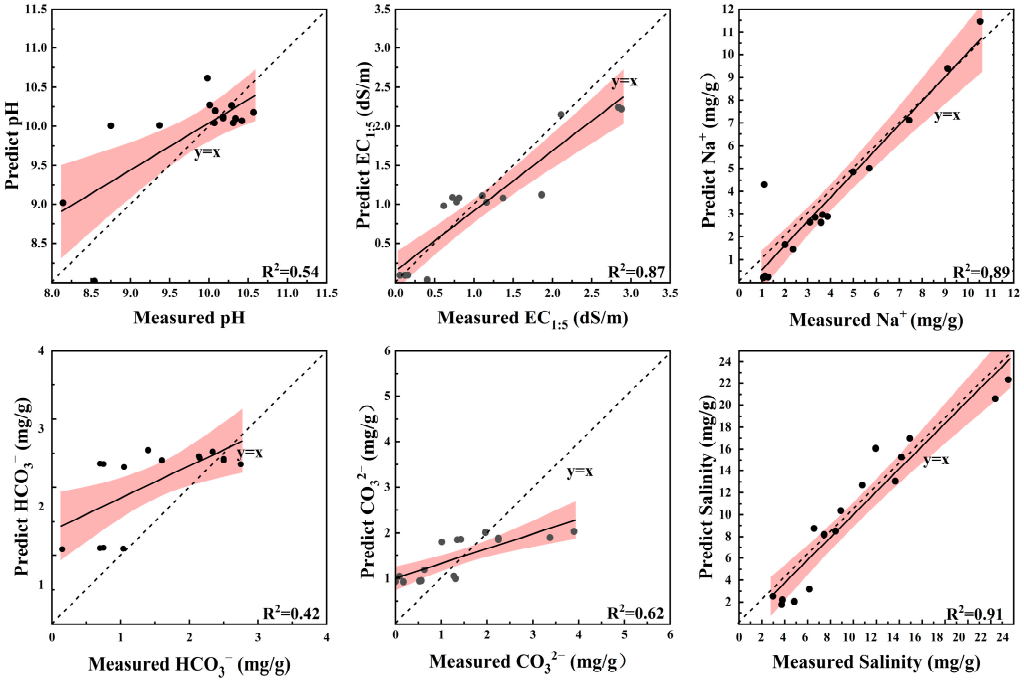

Figure 7. The results of fitting measured and predicted values of a single dependent variable by SEM.

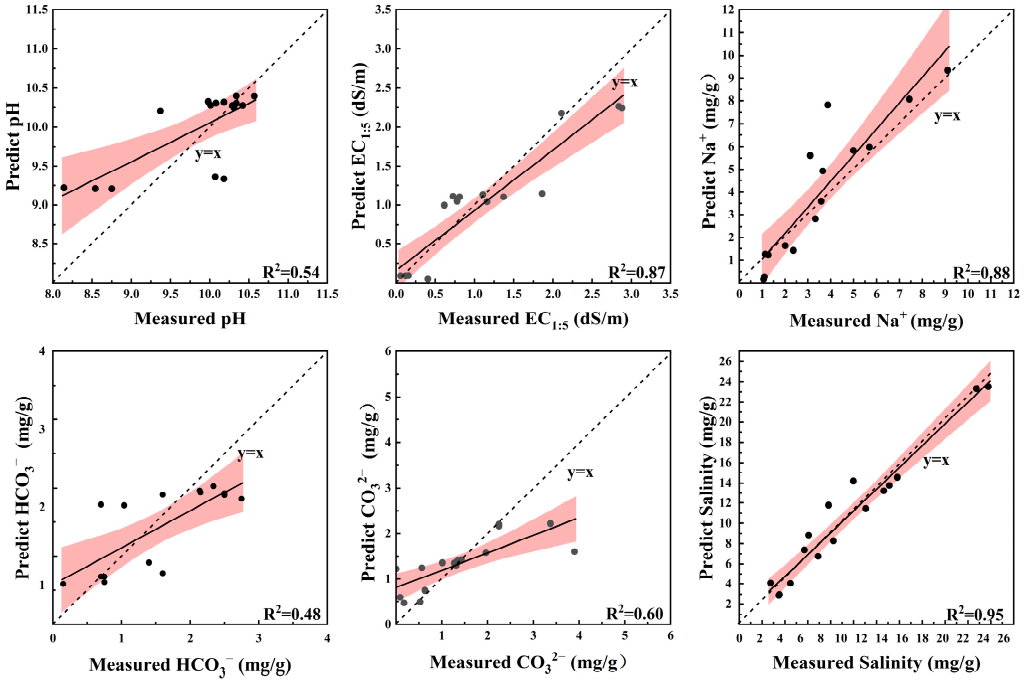

Figure 8. The results of fitting measured and predicted values of a multiple dependent variables by SEM.

Table 7 demonstrates the R^2 and the ratio of performance to deviation (RPD) of the inversion results for different prediction models. From this table, it can be seen that both SEM conditions have good prediction accuracy for most of the salt parameters. In conjunction with the criteria proposed by Farifteh et al. [50], the SEM is good in predicting $EC_{1:5}$, Na^+ and salinity since both inversion models had an R^2 above 0.87 and an RPD above 2.5. Table 7 also indicates that SEMs achieved certain predictive ability for CO_3^{2-} and pH, with an R^2 above 0.5, but the RPD was low, indicating unstable prediction abilities.

Moreover, Table 7 suggests that for most salt parameters, the accuracy of the SEM for single parameter was higher than that of the SEM for multiple parameters.

Table 7. Comparison of inversion accuracy of soil physicochemical parameters.

Method	Index	pH	$EC_{1:5}$ (dS/m)	Na^+ (mg/g)	HCO_3^- (mg/g)	CO_3^{2-} (mg/g)	Salinity (mg/g)
SEM (single)	R^2	0.54	0.87	0.89	0.42	0.62	0.91
	RPD	1.46	2.64	3.08	1.32	1.39	3.24
	RMSE	1.09	0.03	0.38	0.07	0.10	2.14
	MAE	0.66	0.96	2.78	0.93	1.39	2.43
SEM (multiple)	R^2	0.54	0.87	0.88	0.48	0.60	0.95
	RPD	1.47	2.65	2.70	0.73	1.45	4.33
	RMSE	1.03	0.42	0.30	0.54	0.99	1.62
	MAE	0.41	0.57	1.25	0.52	0.82	2.54

N = 17, SEM: Structural equation model.

4. Discussion

Soil cracking is a complex mechanical process that is influenced by various factors, including soil texture, soil chemical properties, and environmental conditions. In this study, the environmental factors, such as temperature and relative humidity during the drying process, were maintained at a constant level, suggesting that the impact of experimental conditions and sample preparation can be disregarded. Moreover, the distribution of soil samples in this study was relatively concentrated, indicating that the samples had similar clay content and mineral types. From the findings presented in Table 4, it can be observed that soil texture had a minimal effect on the desiccation cracking process. The correlation coefficients between clay content and crack characteristics ranged from only 0.13 to 0.26, suggesting a weak relationship. Similar results were reported by Zhang et al. [51] in their study on soda saline–alkali soil in the Songnen Plain. They found that the clay content in the soil ranged from 20% to 29%, which aligns closely with the measurements obtained in this study. They also discovered that the activity index of salt-affected soil in the Songnen Plain ranged from 0.33 to 0.48, indicating that clay particles have little influence on the expansion and contraction of the salt-affected soil in this region. This can be attributed to the predominant presence of illite and montmorillonite mixed layers, with a mixed-layer ratio greater than 50%, along with smaller amounts of illite and kaolinite. Notably, the montmorillonite content, which exhibits the highest activity, is evidently low.

From Table 4, it can be seen that soil salinity plays a very important role in the process of desiccation cracking, which may be attributed to several factors. In soda saline–alkali soils, the presence of exchangeable cations in the salt solution is a crucial factor that determines the physical properties of the soil during the process of dehydration and cracking. This, in turn, influences the cracking of the soil surface due to exposure to salt. From Table 1, it is evident that Na^+ is the predominant cation in the Songnen Plain of China, with a significantly higher content than other types of soil cations. The surface of cohesive saline soil samples generally carries negative charges, which allows for the exchange with exchangeable cations [52]. The alteration in charge distribution further affects the adsorption mechanism of water molecules and consequently leads to changes in their adsorption behavior [53]. Specifically, the arrangement and behavior of water molecules are influenced by cations, particularly Na^+, resulting in the formation of a specific bound water film on the soil surface [54]. This kind of water film acts as a dispersant, increasing the distance between soil particles and reducing their contact and bonding. As a result, the cohesion and tensile strength of the soil are reduced. With the further thickening of the bound water film, soil particles become more susceptible to sliding or separating under stress, leading to a decrease in the overall structural stability and strength of the soil [55–57]. Additionally, the lubricating effect of the bound water film between soil particles decreases the internal friction angle and shear strength of the soil, promoting the desiccation cracking process of salt-affected soils [58]. Moreover, the

content of monovalent Na^+ in the soda saline–alkali soil solution in the Songnen Plain is significantly higher than that of the divalent Ca^{2+} and Mg^{2+}, which can negatively impact the stability of soil aggregates. This weakens the bonding force between soil particles and makes them more easily separated by water, thereby promoting the process of soil surface cracking [59]. In addition, salinity reduces the water absorption capacity of the soil. This may be because clay minerals swell when the concentration of sodium ions in the soil is too high, leading to a reduction in soil pore space. This reduces the rate of water infiltration and permeability and disperses soil particles, further decreasing pores and impeding the flow of water and air. Consequently, the soil becomes more prone to drying and shrinkage, thereby facilitating the process of desiccation cracking [60]. Notably, studies have suggested that the diffuse double layer (DDL) also plays a critical role in the process of desiccation cracking of saline–alkali soils during water evaporation. Specifically, as water evaporates, the DDL thins, reducing the distance between soil particles and facilitating the propagation of desiccation cracks on the soil surface [61]. Therefore, a higher salt content leads to stronger cohesion between soil particles, resulting in increased soil volume shrinkage and more complex soil-cracking phenomena.

It has been shown that the reflectance of salinized soil surface decreases with increasing soil salinity [62,63]. It is also affected by factors such as soil moisture content, surface roughness and organic carbon [64]. Soil cracking increases the roughness condition of the surface, leading to an increase in its scattering at the surface. At the same time, electromagnetic radiation will also cause multiple body scattering in the cracked region, leading to a significant attenuation of electromagnetic radiation energy, suggesting that the presence of cracks significantly reduces the reflectivity of the salinized soil surface. In addition, for samples with different salinity levels, the area of the cracked region increases due to the increasing salinity. The attenuation of electromagnetic radiation is more intense compared to the low-salinity region, which further reduces the spectral reflectance of the samples and also increases the reflectance difference between samples. In the present study, a desiccation cracking experiment was conducted under controlled laboratory conditions. The measurement environment had the same effects on the different samples during the whole drying process, and the moisture content of the samples was so low that its effect on the spectral reflectance can thus be ignored. It was shown that the main factor affecting the spectral reflectance was the salt content. From the correlation curves of spectral reflectance and physicochemical parameters of soil samples, it can be found that the 1990 nm band can be selected as the characteristic band, which corresponds to the similar findings reported by Ren et.al. [22]. Figure 5 indicates that when the salinity increased, the reflectance showed a decreasing trend, which was especially obvious at wavelengths greater than 1400 nm; this finding is consistent with the findings of Wang et al. [65] and Howari et al. [66]. It is because $NaHCO_3$ and Na_2CO_3 are the main components of salt minerals in saline soils. In addition, according to Wang et al. [65], Na_2CO_3 saline soil has the lowest albedo shape compared to Na_2SO_4 saline soil, NaCl saline soil and non-saline soil. Their results also showed that at wavelengths above 1400 nm, reflectance decreased significantly with increasing Na_2CO_3 content. Howari et al. also [66] showed that the sharp decrease in the reflectance of $NaHCO_3$ and Na_2CO_3 with increasing wavelength due to unique resonances induced by stretching and bending can be considered diagnostic. In addition, according to Tedeschi and Dell'Aquila [67] and Huang et al. [68], the aggregation capacity of the soil decreases with soil salinity, probably due to the salt-induced anti-flocculation of the mucilaginous colloids, leading to the inverse ratio of salinity to spectral reflectance. Figure 5 also shows that the soil reflectance tended to increase at 350–1400 nm, while the increase slowed down at 1400–2200 nm and a decreasing trend was observed at 2200–2500 nm. The reason for this is that the reflectance of $NaHCO_3$ in soil shows a significant decreasing trend at wavelengths greater than 1400 nm, and the trend becomes more obvious with the increase in soil salinity.

The use of SEMs has gained significant popularity and has been widely applied in various fields, including the social sciences, economics, and psychology. In recent years,

there has been an increasing interest in using SEMs in the field of soil science [69,70]. In this study, all the regression models developed in Tables 5 and 6 demonstrated high accuracy in modeling the total soil salinity, $EC_{1:5}$, and Na^+ levels. This can be attributed to the fact that Na^+, being the predominant cation in saline–alkali soils of the Songnen Plain, is closely associated with soil salinity. The $EC_{1:5}$ of the soil is mainly influenced by the presence of soluble ions, making it a commonly used indicator for assessing soil salinity in salt-affected soils. These findings highlight the strong predictive capabilities of SEMs for salinity, $EC_{1:5}$, and Na^+. With regards to the prediction of other ions, the overall accuracy of the SEMs displayed a trend, with CO_3^{2-} > HCO_3^- > pH. This can be attributed to the hydrolysis of CO_3^{2-} and HCO_3^- ions in solution, which is often incomplete and reversible. As a result, the content of CO_3^{2-} and HCO_3^- ions remains highly unstable. Additionally, the pH level is directly determined by the OH^- content generated through the hydrolysis of CO_3^{2-} and HCO_3^- ions.

From Tables 1 and 7, it can be seen that the soil samples are very representative, and the model predictions are very close to the actual measurements. In addition, Table 7 also indicates that the SEM is able to combine different crack parameters and spectral responses to quickly and effectively achieve the synchronous prediction of salt parameters, including Na^+, $EC_{1:5}$, and salinity, with desirable prediction accuracy. However, several complex statistical assumptions still need to be clarified and satisfied when an SEM is employed, and multicollinearity and data bias may also affect the precision and explanatory nature of SEMs. In addition, the complexity of SEMs may increase the difficulty and resource requirements for model interpretation, validation, and computation. Therefore, in future studies, both the types of crack parameters and the number of diagnostic spectral bands can be further considered in an attempt to improve the application potential and accuracy of the method in online field measurements of soil salt parameters in the Songnen Plain. Meanwhile, multi-source hyperspectral remote-sensing data from UAV measurements and satellite images can also be added in future studies to realize the high-precision, large-scale and fast-rate inversion of regional soil salinity, thus promoting the application development of soil salinity monitoring using hyperspectral remote sensing.

5. Conclusions

In this study, 57 samples were selected in the Songnen Plain for indoor, controlled soil-cracking experiments in order to study basic information and understand the cracking process of soda saline–alkali soil, in addition to the relationship between soil salt parameters and cracking characterization parameters as well as spectral features. In conclusion, salt content can promote the drying and cracking process due to the interaction of exchangeable cations with soil particles, and a binding water film of large thickness formed among soil particles. Additionally, the main salt parameters, including Na^+, $EC_{1:5}$ and total salinity, can be effectively predicted, combined with the cracking characteristics and spectral responses of the soil surface. Although the SEM method for fitting results of single-parameter prediction has higher accuracy, the SEM method of multi-parameter prediction has a faster processing speed and prediction efficiency. This study therefore provides the possibility to further understand the mechanism of soil cracking and effective measurement methods of salt information in soda saline–alkali soils, which also has great potential for the management of salinized soils and the development of sustainable agriculture.

Author Contributions: Conceptualization, J.R.; methodology, X.L.; software, X.L. and Z.Z.; validation, Z.Z., Y.W. and M.L.; formal analysis, Z.Z. and M.L.; investigation, J.R.; resources, J.R.; data curation, X.L. and M.L.; writing—original draft preparation, X.L.; writing—review and editing, J.R. and Z.Z.; visualization, Y.W.; supervision, M.L.; project administration, J.R.; funding acquisition, J.R. All authors have read and agreed to the published version of the manuscript.

Funding: This research was supported by the Fundamental Research Funds for the Central Universities of China (No. 2022-KYYWF-0156), the Strategic Priority Research Program of the Chinese

Academy of Sciences (No. XDA28110501), and the Natural Science Foundation of Heilongjiang Province of China (No. TD2023D005).

Institutional Review Board Statement: Not applicable.

Data Availability Statement: The data presented in this study are available on request from the corresponding author due to privacy restriction.

Acknowledgments: We authors all appreciate the assistance provided by Zhichun Wang from the Da'an Alkaline Ecological Experimental Station, Chinese Academy of Sciences for the measurements of soil properties, and Xiaojie Li from Northeast Institute of Geography and Agroecology, Chinese Academy of Sciences.

Conflicts of Interest: The authors declare no conflicts of interest.

References

1. Yang, J.; Yao, R.; Wang, X. Research on salt-affected soils in China: History, status quo and prospect. *Acta Pedol. Sin.* **2022**, *59*, 10–27.
2. Boudibi, S.; Sakaa, B.; Benguega, Z.; Fadlaoui, H.; Othman, T.; Bouzidi, N. Spatial prediction and modeling of soil salinity using simple cokriging, artificial neural networks, and support vector machines in El Outaya plain, Biskra, southeastern Algeria. *Acta Geochim.* **2021**, *40*, 390–408. [CrossRef]
3. Seo, B.; Jeong, Y.; Baek, N.; Park, H.; Yang, H.; Park, S.; Choi, W. Soil texture affects the conversion factor of electrical conductivity from 1:5 soil-water to saturated paste extracts. *Pedosphere* **2022**, *32*, 905–915. [CrossRef]
4. Ding, J.; Yu, D. Monitoring and evaluating spatial variability of soil salinity in dry and wet seasons in the Werigan–Kuqa Oasis, China, using remote sensing and electromagnetic induction instruments. *Geoderma* **2014**, *235*, 316–322. [CrossRef]
5. Khadim, F.; Su, H.; Xu, L.; Tian, J. Soil salinity mapping in Everglades National Park using remote sensing techniques and vegetation salt tolerance. *Phys. Chem. Earth* **2019**, *110*, 31–50. [CrossRef]
6. Wang, F.; Yang, S.; Wei, Y.; Shi, Q.; Ding, J. Characterizing soil salinity at multiple depth using electromagnetic induction and remote sensing data with random forest: A case study in Tarim River Basin of southern Xinjiang, China. *Sci. Total Environ.* **2021**, *754*, 142030. [CrossRef]
7. Zarai, B.; Walter, C.; Michot, D.; Montoroi, J.; Hachicha, M. Integrating multiple electromagnetic data to map spatiotemporal variability of soil salinity in Kairouan region, Central Tunisia. *J. Arid Land* **2022**, *14*, 186–202. [CrossRef]
8. Heil, K.; Schmidhalter, U. Comparison of the EM38 and EM38-MK2 electromagnetic induction-based sensors for spatial soil analysis at field scale. *Comput. Electron. Agric.* **2015**, *110*, 267–280. [CrossRef]
9. Khongnawang, T.; Zare, E.; Srihabun, P.; Triantafilis, J. Comparing electromagnetic induction instruments to map soil salinity in two-dimensional cross-sections along the Kham-rean Canal using EM inversion software. *Geoderma* **2020**, *377*, 114611. [CrossRef]
10. Alexakis, D.; Daliakopoulos, I.; Panagea, I.; Tsanis, I. Assessing soil salinity using WorldView-2 multispectral images in Timpaki, Crete, Greece. *Geocarto Int.* **2016**, *33*, 321–338. [CrossRef]
11. Wang, Z.; Zhang, F.; Zhang, X.; Chan, N.; Wang, Y. Regional suitability prediction of soil salinization based on remote-sensing derivatives and optimal spectral index. *Sci. Total Environ.* **2021**, *775*, 145807. [CrossRef] [PubMed]
12. Hu, J.; Peng, J.; Zhou, Y.; Xu, D.; Zhao, R.; Jiang, Q.; Fu, T.; Wang, F.; Shi, Z. Quantitative estimation of soil salinity using UAV-borne hyperspectral and satellite multispectral images. *Remote Sens.* **2019**, *11*, 736. [CrossRef]
13. Mandal, A. The need for the spectral characterization of dominant salts and recommended methods of soil sampling and analysis for the proper spectral evaluation of salt affected soils using hyper-spectral remote sensing. *Remote Sens. Lett.* **2022**, *13*, 588–598. [CrossRef]
14. Das, A.; Bhattacharya, B.; Setia, R.; Jayasree, G.; Das, B. A novel method for detecting soil salinity using AVIRIS-NG imaging spectroscopy and ensemble machine learning. *ISPRS J. Photogramm. Remote Sens.* **2023**, *200*, 191–212. [CrossRef]
15. Moreira, L.; Teixera, A.; Galvao, L. Laboratory salinization of Brazilian alluvial soils and the spectral effects of gypsum. *Remote Sens.* **2014**, *6*, 2647–2663. [CrossRef]
16. Rayhani, M.; Yanful, E.; Fakher, A. Desiccation-induced cracking and its effect on the hydraulic conductivity of clayey soils from Iran. *Can. Geotech. J.* **2007**, *44*, 276–283. [CrossRef]
17. Chen, A.; Zhang, D.; Lei, B.; Yang, Y.; Liu, G. Effects of contraction and deformation of vertisol on its crack development and shear strength in Yuanmou Dry-Hot Valley. *Chin. J. Soil Sci.* **2015**, *46*, 341–347.
18. Cheng, Q.; Tang, C.; Chen, Z.; El-Maarry, M.; Zeng, H.; Shi, B. Tensile behavior of clayey soils during desiccation cracking process. *Eng. Geol.* **2020**, *279*, 105909. [CrossRef]
19. Albrecht, B.; Benson, C. Effect of desiccation on compacted natural clays. *J. Geotech. Geoenviron. Eng.* **2001**, *127*, 67–75. [CrossRef]
20. Puppala, A.; Manosuthikij, T.; Chittoori, B. Swell and shrinkage characterizations of unsaturated expansive clays from Texas. *Eng. Geol.* **2013**, *164*, 187–194. [CrossRef]
21. Vail, M.; Zhu, C.; Tang, C.; Anderson, L.; Moroski, M.; Montalbo-Lomboy, M. Desiccation cracking behavior of MICP-treated bentonite. *Geosciences* **2019**, *9*, 385. [CrossRef]

22. Ren, J.; Chen, Q.; Ma, D.; Xie, R.; Zhu, H.; Zang, S. Study on a fast EC measurement method of soda saline-alkali soil based on wavelet decomposition texture feature. *Catena* **2021**, *203*, 105272. [CrossRef]
23. Zhang, Z.; Li, X.; Zhou, S.; Zhao, Y.; Ren, J. Quantitative Study on Salinity Estimation of Salt-Affected Soils by Combining Different Types of Crack Characteristics Using Ground-Based Remote Sensing Observation. *Remote Sens.* **2023**, *15*, 3249. [CrossRef]
24. Fujimaki, H.; Abd El Baki, H. Effect of bypass-flow on leaching of salts in a cracking soil in the nile delta. *Water* **2021**, *13*, 993. [CrossRef]
25. Zhang, X.; Chen, Y.; Ye, W.; Cui, Y.; Deng, Y.; Chen, B. Effect of salt concentration on desiccation cracking behavior of GMZ bentonite. *Environ. Earth Sci.* **2017**, *76*, 531. [CrossRef]
26. Xing, X.; Jing, X.; Zhao, F.; Wang, W. Interactions between water evaporation and surface cracking in NaCl-induced homogeneous silt loam and sand. Commun. *Soil Sci. Plant Anal.* **2022**, *53*, 1930–1941. [CrossRef]
27. Wang, C.; Feng, G.; Zhang, Z.; Huang, M.; Qi, W.; Ma, L. Geometrical and statistical analysis of dynamic crack morphology in shrink-swell soils with addition of maize roots or salinity (NaCl). *Soil Till. Res.* **2021**, *212*, 105057. [CrossRef]
28. Yu, H.; Wang, Z.; Mao, D.; Jia, M.; Chang, S.; Li, X. Spatiotemporal variations of soil salinization in China's West Songnen Plain. *Land Degrad. Dev.* **2023**, *34*, 2366–2378. [CrossRef]
29. Li, X.; Sun, Y.; Chen, X.; Li, Y.; Jiang, T.; Liang, Z. Saline-sodic soil EC retrieval based on box-cox transformation and machine learning. *IEEE J. Sel. Top. Appl. Earth Obs. Remote Sens.* **2022**, *15*, 1692–1700. [CrossRef]
30. Yao, D.; Liao, Y.; Kong, X. Characteristics of saline-alkali land and resources based on three-layer fusion of saline-alkali soil in Songnen Plain of China. *Trans. Chin. Soc. Agric. Eng.* **2022**, *38*, 247–257.
31. Wang, S.; Sun, L.; Ling, N.; Zhu, C.; Chi, F.; Li, W.; Hao, X.; Zhang, W.; Bian, J.; Chen, L. Exploring soil factors determining composition and structure of the bacterial communities in saline-alkali soils of Songnen Plain. *Front. Microbiol.* **2020**, *10*, 2902. [CrossRef]
32. Bao, S. *Agricultural Chemistry Analysis of Soils*; Agriculture Press: Beijing, China, 2000.
33. Tran, D.; Ralaizafisoloarivony, N.; Charlier, R.; Mercatoris, B.; Léonard, A.; Toye, D.; Degré, A. Studying the effect of desiccation cracking on the evaporation process of a Luvisol–From a small-scale experimental and numerical approach. *Soil Till. Res.* **2019**, *193*, 142–152. [CrossRef]
34. Ren, J.; Li, X.; Zhao, K.; Fu, B.; Jiang, T. Study of an on-line measurement method for the salt parameters of soda-saline soils based on the texture features of cracks. *Geoderma* **2016**, *263*, 60–69. [CrossRef]
35. Ren, J.; Xie, R.; Zhu, H.; Zhao, Y.; Zhang, Z. Comparative study on the abilities of different crack parameters to estimate the salinity of soda saline-alkali soil in Songnen Plain, China. *Catena* **2022**, *213*, 106221. [CrossRef]
36. Li, D.; Yang, B.; Yang, C.; Zhang, Z.; Hu, M. Effects of salt content on desiccation cracks in the clay. *Environ. Earth Sci.* **2021**, *80*, 671. [CrossRef]
37. Wan, Y.; Wu, C.; Xue, Q.; Hui, X. Effects of plastic contamination on water evaporation and desiccation cracking in soil. *Sci. Total Environ.* **2019**, *654*, 576–582. [CrossRef]
38. Bordoloi, S.; Ni, J.; Ng, C. Soil desiccation cracking and its characterization in vegetated soil: A perspective review. *Sci. Total Environ.* **2020**, *729*, 138760. [CrossRef] [PubMed]
39. Aouat, S.; Ait-hammi, I.; Hamouchene, I. A new approach for texture segmentation based on the Gray Level Co-occurrence Matrix. *Multimed Tools Appl.* **2021**, *80*, 24027–24052. [CrossRef]
40. Gupta, C.; Gondhi, N.; Lehana, P. Gray level co-occurrence matrix (GLCM) parameters analysis for pyoderma image variants. *J. Comput. Theor. Nanosci.* **2020**, *17*, 353–358. [CrossRef]
41. Haralick, R.; Shanmugam, K.; Dinstein, I. Textural features for image classification. *IEEE Trans. Syst. Man Cybern.* **1973**, *6*, 610–621. [CrossRef]
42. Rosseel, Y. lavaan: An R package for structural equation modeling. *J. Stat. Softw.* **2012**, *48*, 1–36. [CrossRef]
43. Elshaer, I.; Alrawad, M.; Lutfi, A.; Azazz, A. Social commerce and buying intention post COVID-19: Evidence from a hybrid approach based on SEM–fsQCA. *J. Retail. Consum. Serv.* **2024**, *76*, 103548. [CrossRef]
44. Lubinski, D. Introduction to the special section on cognitive abilities: 100 years after Spearman's (1904) "'General intelligence', objectively determined and measured". *J. Abnorm. Soc. Psychol.* **2004**, *86*, 96. [CrossRef]
45. Yang, L.; Shen, F.; Zhang, L.; Cai, Y.; Yi, F.; Zhou, C. Quantifying influences of natural and anthropogenic factors on vegetation changes using structural equation modeling: A case study in Jiangsu Province, China. *J. Clean. Prod.* **2021**, *280*, 124330. [CrossRef]
46. Wang, M.; Zhang, C.; Chen, S.; Zhang, Y.; Yu, T.; Xue, X.; Wu, L.; Zhou, W.; Yun, X.; Yan, R. Moderate grazing increased carbon, nitrogen and phosphorus storage in plants and soil in the Eurasian meadow steppe ecosystem. *Sci. Total Environ.* **2024**, *914*, 169864. [CrossRef]
47. Yang, L.; Hu, X.; Chang, Z.; Song, H.; Li, T.; Li, L. The Effects of Various Long-Term Fertilizer Applications on Soil Carbon Fractions in a Winter Wheat Monoculture Area. *Agronomy* **2023**, *14*, 82. [CrossRef]
48. Blanthorne, C.; Jonesfarmer, L.; Almer, E. Why you should consider SEM: A guide to getting started. *Adv. Account. Behav. Res.* **2006**, *9*, 179–207.
49. Gogtay, N.; Thatte, U. Principles of correlation analysis. *J. Assoc. Phys. India* **2017**, *65*, 78–81.
50. Farifteh, J.; Farshad, A.; George, R. Assessing salt-affected soils using remote sensing, solute modelling, and geophysics. *Geoderma* **2006**, *130*, 191–206. [CrossRef]

51. Zhang, G.; Yu, Q.; Wei, G.; Chen, B.; Yang, L.; Hu, C.; Li, J.; Chen, H. Basic property of Songnen plain saline-alkali soil. *Hydrogeol. Eng. Geol.* **2007**, *2*, 37–40. (In Chinese)
52. Aboudi, M.; Hanafiah, M.; Chowdhury, A. Environmental characteristics of clay and clay-based minerals. *GeoloGy Ecol. Landsc.* **2017**, *1*, 155–161. [CrossRef]
53. Chorom, M.; Rengasamy, P. Dispersion and zeta potential of pure clays as related to net particle charge under varying pH, electrolyte concentration and cation type. *Eur. J. Soil Sci.* **1995**, *46*, 657–665. [CrossRef]
54. Khorshidi, M.; Lu, N.; Khorshidi, A. Intrinsic relationship between matric potential and cation hydration. *Vadose Zone J.* **2016**, *15*, 1–12. [CrossRef]
55. DeCarlo, K.; Shokri, N. Salinity effects on cracking morphology and dynamics in 3-D desiccating clays. *Water Resour. Res.* **2014**, *50*, 3052–3072. [CrossRef]
56. Wang, J.; Chai, J.; Xu, Z.; Geng, K.; Zhang, P. A review of barrier properties of polymer-modified bentonite applied to vertical cutoff walls under dry-wet cycling and chemical erosion. *J. Water Process Eng.* **2024**, *65*, 105759. [CrossRef]
57. Yang, B.; Yuan, J. Influence of soda content on desiccation cracks in clayey soils. *Soil Sci. Soc. Am. J.* **2019**, *83*, 1054–1061. [CrossRef]
58. Jeong, S.W.; Locat, J.; Leroueil, S. The effect of salinity and shear history on the rheological characteristics of illite-rich and Na-montmorillonite-rich clays. *Clay Clay Miner.* **2012**, *60*, 108–120. [CrossRef]
59. Yan, S.; Zhang, T.; Zhang, B.; Liu, Z.; Cheng, Y.; Feng, H. Cation composition of saline water affects soil structure by altering the formation of macropores and cracks in illite soils. *Soil Till. Res.* **2024**, *239*, 106052. [CrossRef]
60. Qadir, M.; Schubert, S. Degradation processes and nutrient constraints in sodic soils. *Land Degrad. Dev.* **2002**, *13*, 275–294. [CrossRef]
61. Shokri, N.; Zhou, P.; Keshmiri, A. Patterns of desiccation cracks in saline bentonite layers. *Transp. Porous Media* **2015**, *110*, 333–344. [CrossRef]
62. Wang, L.; Zhang, B.; Shen, Q.; Yao, Y.; Zhang, S.; Wei, H.; Yao, R.; Zhang, Y. Estimation of soil salt and ion contents based on hyperspectral remote sensing data: A case study of baidunzi basin, China. *Water* **2021**, *13*, 559. [CrossRef]
63. Al-Jubouri, A.; Wheib, K. Effect of soil salinity on spectral reflectance of red and NIR wavelengths in AL-Salamiyat project. *Plant Arch.* **2020**, *20*, 1359–1365.
64. Wu, C.; Zheng, Y.; Yang, H.; Yang, Y.; Wu, Z. Effects of different particle sizes on the spectral prediction of soil organic matter. *Catena* **2021**, *196*, 104933. [CrossRef]
65. Wang, Q.; Li, P.; Chen, X. Modeling salinity effects on soil reflectance under various moisture conditions and its inverse application: A laboratory experiment. *Geoderma* **2012**, *170*, 103–111. [CrossRef]
66. Howari, F.; Goodell, P.; Miyamoto, S. Spectral properties of salt crusts formed on saline soils. *J. Environ. Qual.* **2002**, *31*, 1453–1461. [CrossRef] [PubMed]
67. Tedeschi, A.; Dell'Aquila, R. Effects of irrigation with saline waters, at different concentrations, on soil physical and chemical characteristics. *Agric. Water Manag.* **2005**, *77*, 308–322. [CrossRef]
68. Huang, C.; Xue, X.; Wang, T.; De Mascellis, R.; Mele, G.; You, Q.; Peng, F.; Tedeschi, A. Effects of saline water irrigation on soil properties in northwest China. *Environ. Earth Sci.* **2011**, *63*, 701–708. [CrossRef]
69. Angelini, M.; Heuvelink, G.; Kempen, B. Multivariate mapping of soil with structural equation modelling. *Eur. J. Soil Sci.* **2017**, *68*, 575–591. [CrossRef]
70. Angelini, M.; Kempen, B.; Heuvelink, G.; Temme, A.; Ransom, M. Extrapolation of a structural equation model for digital soil mapping. *Geoderma* **2020**, *367*, 114226. [CrossRef]